Deformation estimation of a circular tunnel from a point cloud using elliptic Fourier analysis

Naotoshi Yasuda[a,*], Ying Cui[b]

[a] *Department of Civil and Earth Resources Engineering, Kyoto University, Nishikyo-ku, Kyoto, 615-8530, Kyoto, Japan*
[b] *Department of Civil Engineering, Yokohama National University, Hodogaya, Yokohama, 240-8501, Kanagawa, Japan*

Abstract

In recent years, light detection and ranging technology has been applied to tunnel engineering. Although more accurate than traditional measurement techniques, estimating the tunnel deformation from the light detection and ranging point cloud remains challenging. This paper proposes a deformation estimation method using elliptic Fourier analysis, whereby the tunnel deformation is estimated from the difference in the Fourier series representations of the tunnel outline before and after deformation. The applicability of the proposed method for a circular tunnel cross-section is theoretically considered. Numerical results show that there is almost no error in the estimation of radial displacement, regardless of the measurement conditions. In contrast, there is an error in the estimation of circumferential displacement because this does not modify the circular tunnel outline. Therefore, tunnel deformation cannot be accurately estimated using point cloud data obtained only from distance measurements. As a special case, when the full-slip condition is imposed on the ground–lining interface and the estimated circumferential displacement of the inner surface is regarded as that of the middle surface, circumferential displacement can also be accurately estimated. Moreover, the difference in the deformation patterns under the full-slip and no-slip conditions decreases as the relative stiffness of the lining with respect to the ground increases. As a result, the deformation estimation accuracy is expected to be high for tunnels with a high possibility of deformation. When

[*] Corresponding author. Tel.:+81 75 383 7558; Fax: +81 75 383 3114
Email address: yasuda.naotoshi.3x@kyoto-u.ac.jp (Naotoshi Yasuda)

the distance measurement error is considered, the estimation accuracy of the displacement decreases, especially that of the circumferential displacement. Smoothed data significantly improve the accuracy, and high-precision estimation can be achieved when the measurement error is small compared with the tunnel deformation. However, small displacement errors produce significant stress errors in the higher-order terms of the Fourier series. Therefore, only the lower-order terms can be used for stress estimations.

Keywords:
Elliptic Fourier analysis, Tunnel, Point cloud, Deformation, Laser scanning

---

1. Introduction

Displacement measurements have been used for many years to evaluate the deformation of tunnels during their construction and operation phases. Tape extensometers and total stations can monitor changes in relative displacement between specified points, though it is difficult to estimate the overall deformation of the tunnel structure accurately because only a limited number of points can be monitored in a tunnel cross-section.

In recent years, light detection and ranging (LiDAR) technology has been applied to tunnel engineering (Yoon et al., 2009; Fekete et al., 2010; Lato and Diederichs, 2014; Nuttens et al., 2014; Puente et al., 2016; Farahani et al., 2019; Xu et al., 2019; Jiang et al., 2020; Xie et al., 2021). The resulting point cloud, which is the set of 3D coordinate data, can be used to estimate the 3D profile of the tunnel. Using LiDAR technology, the overall deformation of the tunnel structure can be estimated with better accuracy than when using traditional measurements. Nevertheless, forming accurate estimations of the tunnel deformation from changes in the profiles obtained by the laser measurements remains challenging, because the measurements do not track the movement of points. The actual deformation cannot be estimated from the changes in profiles without some additional assumptions.

Han et al. (2013b,a) proposed a minimum-distance projection (MDP) algorithm to identify possible deformations. This method is intuitive and straightforward, although the validity of the deformation estimated by the MDP algorithm is unclear. Walton et al. (2014) developed an elliptical fitting algorithm that offers improved change-detection capabilities when applied to the deformation monitoring of a circular tunnel. Xie and Lu (2017) established a 3D modeling algorithm that processes the point cloud of a circular tunnel and displays its relative deformation, including settlement, segment dislocation, and cross-section convergence, while Cui et al. (2019) proposed a stepwise ellipse fitting method for the cross-section of a non-perfect circular tunnel. These methods focus on assessing the ovaling deformation, which is the most typical tunnel deformation.

Elliptical Fourier analysis (EFA) is a mathematical tool developed by Kuhl and Giardina (1982) to describe a closed outline quantitatively using a Fourier series expansion. This method is considered to be a more generalized method of ellipse fitting. Moreover, its theoretical applicability to tunnel deformation modeling deserves consideration, because general elasticity solutions are expressed in a similar series expansion (Timoshenko and Goodier, 1951; Einstein and Schwartz, 1979; Yasuda et al., 2017).

This paper proposes a deformation estimation method based on a set of data points in space obtained on the lining surface using EFA. The applicability of the proposed method for a circular tunnel cross-section is theoretically considered, and the effect of distance measurement errors on the estimation accuracy is investigated.

2. Theory

2.1. Problem definition

Consider an infinitely long lined circular tunnel with the center $O(0, 0)$, as shown in Figure. A.1. The tunnel is assumed to be located sufficiently deep below the ground surface and is under a far-field stress state defined by the vertical component p and horizontal component kp, where k is the coefficient of lateral pressure. Compression is taken to be positive, and it is assumed that p and kp are imposed after the construction of the lining. The surrounding ground is considered to be an infinite elastic, homogeneous, isotropic medium. The lining is treated as an elastic, homogeneous, isotropic medium with an inner radius of R and a thickness of h.

The measurement position is $O^{\mathrm{obs}}(x^{\mathrm{obs}}, y^{\mathrm{obs}})$. R_i^{obs} is the measured distance from the measurement position O^{obs} to the i-th measurement point $P_i(x_i, y_i)$. The first measurement point P_1 is assumed to be on the positive x-axis. The total number of measurement points is K, which is assumed to be an odd number. θ_0^{obs} is the measured angle between the line segment

$O^{\text{obs}}y^{\text{obs}}$ and $O^{\text{obs}}P_1$, and is expressed as follows:

$$\theta_0^{\text{obs}} = \tan^{-1}\left(\frac{-y^{\text{obs}}}{R - x^{\text{obs}}}\right). \tag{1}$$

θ_i^{obs} is the measured angle between the line segment $O^{\text{obs}}P_1$ and $O^{\text{obs}}P_i$, and is given by

$$\theta_i^{\text{obs}} = \frac{2\pi(i-1)}{K}. \tag{2}$$

For simplicity, the angles are assumed to be evenly spaced, although θ_i^{obs} can be chosen arbitrarily.

2.2. Fourier series representation of a tunnel outline before deformation

The i-th measurement point P_i lies at the intersection of a circle and a straight line. The equation of the circle is

$$\left.\begin{aligned} x &= R\cos\theta \\ y &= R\sin\theta \end{aligned}\right\}, \tag{3}$$

and the equation of the line is

$$y = \tan\left(\theta_0^{\text{obs}} + \theta_i^{\text{obs}}\right)\left(x - x^{\text{obs}}\right) + y^{\text{obs}}. \tag{4}$$

From Eqs. (3) and (4), the intersection points from P_1 to P_K can be derived analytically. The difference in the x-direction, Δx_i, the difference in the y-direction, Δy_i, and the distance between the two intersection points, $\Delta \ell_i$, are given by

$$\Delta x_i = \begin{cases} x_1 - x_K, & (i = K) \\ x_{i+1} - x_i, & (otherwise) \end{cases} \tag{5}$$

$$\Delta y_i = \begin{cases} y_1 - y_K, & (i = K) \\ y_{i+1} - y_i, & (otherwise) \end{cases} \tag{6}$$

$$\Delta \ell_i = \sqrt{\Delta x_i^2 + \Delta y_i^2}. \tag{7}$$

In EFA, any two-dimensional outline is approximated with a polygon by connecting the measurement points with straight lines. The sum of the line segments from measurement point P_1 to P_{i+1}, ℓ_i, and the total length of the outline, L, are

$$\ell_i = \begin{cases} 0, & (i = 0) \\ \sum_{I=1}^{i} \Delta\ell_I, & (otherwise) \end{cases} \tag{8}$$

$$L = \ell_K = \sum_{i=1}^{K} \Delta\ell_i. \tag{9}$$

For a truncated harmonic series containing N terms, the coordinates of the estimated outline can be expanded in parametric form as follows:

$$x(\ell) = A_0 + \sum_{n=1}^{N} \left(a_n \cos \frac{2n\pi\ell}{L} + b_n \sin \frac{2n\pi\ell}{L} \right), \tag{10}$$

$$y(\ell) = C_0 + \sum_{n=1}^{N} \left(c_n \cos \frac{2n\pi\ell}{L} + d_n \sin \frac{2n\pi\ell}{L} \right), \tag{11}$$

with

$$N = \frac{K-1}{2}, \tag{12}$$

$$A_0 = x_1 - \sum_{n=1}^{N} a_n, \tag{13}$$

$$C_0 = y_1 - \sum_{n=1}^{N} c_n. \tag{14}$$

The four coefficients of the n-th elliptic harmonic term (Kuhl and Giardina, 1982; Lestrel, 1989) are obtained as

$$a_n = \frac{L}{2n^2\pi^2} \sum_{i=1}^{K} \frac{\Delta x_i}{\Delta \ell_i} \left(\cos \frac{2n\pi\ell_i}{L} - \cos \frac{2n\pi\ell_{i-1}}{L} \right), \tag{15}$$

$$b_n = \frac{L}{2n^2\pi^2} \sum_{i=1}^{K} \frac{\Delta x_i}{\Delta \ell_i} \left(\sin \frac{2n\pi\ell_i}{L} - \sin \frac{2n\pi\ell_{i-1}}{L} \right), \tag{16}$$

$$c_n = \frac{L}{2n^2\pi^2} \sum_{i=1}^{K} \frac{\Delta y_i}{\Delta \ell_i} \left(\cos \frac{2n\pi\ell_i}{L} - \cos \frac{2n\pi\ell_{i-1}}{L} \right), \tag{17}$$

$$d_n = \frac{L}{2n^2\pi^2} \sum_{i=1}^{K} \frac{\Delta y_i}{\Delta \ell_i} \left(\sin \frac{2n\pi\ell_i}{L} - \sin \frac{2n\pi\ell_{i-1}}{L} \right). \tag{18}$$

As the total number of measurement points K approaches infinity, the total length of the outline L and the variable representing the position on the closed outline ℓ_i approach $2\pi R$ and $R\theta$, respectively. Thus, the variable $2n\pi\ell_i/L$ approaches $n\theta$.

2.3. Fourier series representation of the tunnel outline after deformation

Tunnel surface deformation can be approximately expressed as follows:

$$u_r(\theta) = U_{r,0} + \sum_{n=1}^{N} \left(U^{\mathrm{c}}_{r,n} \cos n\theta + U^{\mathrm{s}}_{r,n} \sin n\theta \right), \tag{19}$$

$$u_\theta(\theta) = U_{\theta,0} + \sum_{n=1}^{N} \left(U^{\mathrm{c}}_{\theta,n} \cos n\theta + U^{\mathrm{s}}_{\theta,n} \sin n\theta \right), \tag{20}$$

where $U_{r,0}$, $U^{\mathrm{c}}_{r,n}$, $U^{\mathrm{s}}_{r,n}$, $U_{\theta,0}$, $U^{\mathrm{c}}_{\theta,n}$, and $U^{\mathrm{s}}_{\theta,n}$ are constants. The displacement can be converted from polar to Cartesian coordinates using the transform

$$\begin{pmatrix} u_x \\ u_y \end{pmatrix} = \begin{pmatrix} \cos\theta & -\sin\theta \\ \sin\theta & \cos\theta \end{pmatrix} \begin{pmatrix} u_r \\ u_\theta \end{pmatrix}. \tag{21}$$

As a result, the displacement in Cartesian coordinates can be expressed as follows:

$$u_x(\theta) = U_{x,0} + \sum_{n=1}^{N} \left(U^{\mathrm{c}}_{x,n} \cos n\theta + U^{\mathrm{s}}_{x,n} \sin n\theta \right), \tag{22}$$

$$u_y(\theta) = U_{y,0} + \sum_{n=1}^{N} \left(U^{\mathrm{c}}_{y,n} \cos n\theta + U^{\mathrm{s}}_{y,n} \sin n\theta \right), \tag{23}$$

where $U_{x,0}$, $U^{\mathrm{c}}_{x,n}$, $U^{\mathrm{s}}_{x,n}$, $U_{y,0}$, $U^{\mathrm{c}}_{y,n}$, and $U^{\mathrm{s}}_{y,n}$ are constants.

The i-th measurement point P'_i is defined as the intersection of the deformed circular tunnel and a straight line, where the prime is used to denote variables after tunnel deformation. The equation of the deformed tunnel is

$$\left.\begin{aligned} x' &= R\cos\theta + u_x(\theta) \\ y' &= R\sin\theta + u_y(\theta) \end{aligned}\right\}, \tag{24}$$

and the equation of the line is

$$y' = \tan\left(\theta_0^{\mathrm{obs}} + \theta_i^{\mathrm{obs}}\right)\left(x' - x^{\mathrm{obs}}\right) + y^{\mathrm{obs}}. \tag{25}$$

From Eqs. (24) and (25), the intersection points from P'_1 to P'_K can be obtained numerically.

The coordinates of the estimated outline after tunnel deformation can be expanded in a similar form to Eqs. (10) and (11):

$$x'(\ell') = A'_0 + \sum_{n=1}^{N}\left(a'_n \cos\frac{2n\pi\ell'}{L'} + b'_n \sin\frac{2n\pi\ell'}{L'}\right), \tag{26}$$

$$y'(\ell') = C'_0 + \sum_{n=1}^{N}\left(c'_n \cos\frac{2n\pi\ell'}{L'} + d'_n \sin\frac{2n\pi\ell'}{L'}\right). \tag{27}$$

2.4. Deformation estimation

The magnitude of tunnel deformation is considerably smaller than the tunnel radius R. Assuming that the relative position on the closed line does not change before and after tunnel deformation (that is, the assumption $\ell/L \approx \ell'/L'$ holds), the estimated deformation can be expressed by the following equations:

$$u_x^{\mathrm{est}}(\ell) \approx (A'_0 - A_0) + \sum_{n=1}^{N}\left\{(a'_n - a_n)\cos\frac{2n\pi\ell}{L} + (b'_n - b_n)\sin\frac{2n\pi\ell}{L}\right\}, \tag{28}$$

$$u_y^{\mathrm{est}}(\ell) \approx (C'_0 - C_0) + \sum_{n=1}^{N}\left\{(c'_n - c_n)\cos\frac{2n\pi\ell}{L} + (d'_n - d_n)\sin\frac{2n\pi\ell}{L}\right\}. \tag{29}$$

In this paper, to enable comparisons with the theoretical solution, Eqs. (28)

and (29) are further approximated as follows:

$$u_x^{\mathrm{est}}(\theta) = (A'_0 - A_0) + \sum_{n=1}^{N} \{(a'_n - a_n)\cos n\theta + (b'_n - b_n)\sin n\theta\}, \tag{30}$$

$$u_y^{\mathrm{est}}(\theta) = (C'_0 - C_0) + \sum_{n=1}^{N} \{(c'_n - c_n)\cos n\theta + (d'_n - d_n)\sin n\theta\}. \tag{31}$$

These expressions can be written in polar coordinates as

$$u_r^{\mathrm{est}}(\theta) = U_{r,0}^{\mathrm{est}} + \sum_{n=1}^{N} \left(U_{r,n}^{\mathrm{est,c}} \cos n\theta + U_{r,n}^{\mathrm{est,s}} \sin n\theta\right), \tag{32}$$

$$u_\theta^{\mathrm{est}}(\theta) = U_{\theta,0}^{\mathrm{est}} + \sum_{n=1}^{N} \left(U_{\theta,n}^{\mathrm{est,c}} \cos n\theta + U_{\theta,n}^{\mathrm{est,s}} \sin n\theta\right), \tag{33}$$

where $U_{r,0}^{\mathrm{est}}$, $U_{r,n}^{\mathrm{est,c}}$, $U_{r,n}^{\mathrm{est,s}}$, $U_{\theta,0}^{\mathrm{est}}$, $U_{\theta,n}^{\mathrm{est,c}}$, and $U_{\theta,n}^{\mathrm{est,s}}$ are constants.

2.5. Circumferential stress of the lining

For simplicity, the lining is treated as an elastic cylindrical shell of thickness h. The mean radius of the lining R_{mid} is $R + h/2$. The conversion from the displacement of the inner surface, which is obtained from the measurements, to that of the middle surface is given by the following equation (Flügge, 1973):

$$u_{r,\mathrm{mid}} = u_r, \tag{34}$$

$$u_{\theta,\mathrm{mid}} = \frac{2R+h}{2R}\left(u_\theta - \frac{h}{2R+h}\frac{du_r}{d\theta}\right). \tag{35}$$

The radial displacement does not change in the direction of the thickness of the lining.

The axial thrust $n_{\theta\theta}$ and the bending moment $m_{\theta\theta}$ of the lining can be calculated from the displacement of the middle surface. These quantities can be expressed as follows (Flügge, 1973):

$$\begin{pmatrix} n_{\theta\theta} \\ m_{\theta\theta} \end{pmatrix} = \begin{pmatrix} \frac{D_\ell}{R_{\mathrm{mid}}} + \frac{K_\ell}{R_{\mathrm{mid}}^3}\left(1 + \frac{d^2}{d\theta^2}\right) & \frac{D_\ell}{R_{\mathrm{mid}}}\frac{d}{d\theta} \\ \frac{K_\ell}{R_{\mathrm{mid}}^2}\left(1 + \frac{d^2}{d\theta^2}\right) & 0 \end{pmatrix} \begin{pmatrix} u_{r,\mathrm{mid}} \\ u_{\theta,\mathrm{mid}} \end{pmatrix}, \tag{36}$$

with:

$$D_\ell = \frac{E_\ell h}{1 - \nu_\ell^2}, \tag{37}$$

$$K_\ell = \frac{E_\ell h^3}{12(1 - \nu_\ell^2)}. \tag{38}$$

D_ℓ, K_ℓ are the extensional rigidity and flexural rigidity of the lining, respectively, and E_ℓ, ν_ℓ are the Young's modulus and Poisson's ratio of the lining, respectively.

The circumferential stress at the surface of the lining, $\sigma_{\theta\theta}$, can be approximated from $n_{\theta\theta}$ and $m_{\theta\theta}$ as follows:

$$\sigma_{\theta\theta} = \frac{n_{\theta\theta}}{h} \pm \frac{h m_{\theta\theta}}{2I}, \tag{39}$$

with:

$$I = \frac{h^3}{12}, \tag{40}$$

where I is the moment of inertia of the lining. The $\pm$ sign in Eq. (39) denotes that the upper side is chosen for the inner surface and the lower side is chosen for the outer surface.

3. Numerical results

The material properties used for the following calculations are given in Table A.1. The tunnel radius is 5.0 m and the lining thickness is 10% of that. As a basic case, soft ground is assumed because it often causes problems with the lining. The Young's modulus of the ground E_g is assumed to be 0.30 GPa, which is 1% of that of the concrete lining. The i-th measurement point P_i', which is obtained by solving Eqs. (24) and (25) simultaneously, is derived using a numerical solver (vpasolve) in MATLAB. Either the no-slip (no relative shear displacement) or full-slip (no shear stress transmission) condition is imposed on the ground–lining interface to derive the theoretical deformation expressed by Eqs. (19) and (20). Details regarding the calculation of the deformation can be found in Yasuda et al. (2017). The first 51 terms of the series are used to obtain the following estimates (the upper limit of summation N is assumed to be 50 in Eqs. (32) and (33)).

Figure A.2 shows the estimated displacement distribution for two kinds of measurement positions: $O^{\text{obs}}(0,0)$, at the center of the tunnel, and $O^{\text{obs}}(-3,-3)$, which is close to the tunnel wall. The $\boldsymbol{u}$ is the given displacement vector expressed by Eqs. (22) and (23), and the $\boldsymbol{u}^{\text{est}}$ is the estimated displacement vector expressed by Eqs. (30) and (31). The displacement has been magnified by a factor of 500. The Young's modulus of the ground E_g, the vertical pressure p, and the coefficient of lateral pressure k are 0.30 GPa, 0.10 MPa, and 0.50, respectively. The total number of measurement points K is 1001. The no-slip condition is imposed on the ground–lining interface. At measurement position $O^{\text{obs}}(0,0)$, the given displacement vector $\boldsymbol{u}$ and the estimated displacement vector $\boldsymbol{u}^{\text{est}}$ are in good agreement. In contrast, in the case of $O^{\text{obs}}(-3,-3)$, $\boldsymbol{u}^{\text{est}}$ is shifted in a counterclockwise direction. Figure A.3 presents the results of Fig. A.2 in terms of radial and circumferential displacement. The u_r and u_θ are expressed by Eqs. (19) and (20), the u_r^{est} and u_θ^{est} are expressed by Eqs. (32) and (33), and the $u_{\theta,\text{mid}}$ are expressed by Eq. (35). In addition, in the case of $O^{\text{obs}}(-3,-3)$, a modified estimated circumferential displacement in which the rigid body rotation component $U_{\theta,0}^{\text{est}}$ is set to zero is plotted. In both cases, there is no difference in the distribution of u_r and u_r^{est}. In contrast, there is a difference in the distribution of u_θ and u_θ^{est}, especially at $O^{\text{obs}}(-3,-3)$. At $O^{\text{obs}}(0,0)$, u_θ^{est} is closer to $u_{\theta,\text{mid}}$ than to u_θ, although u_θ^{est} should be closer to u_θ. The distribution of u_θ^{est} at both measurement points is in agreement when $U_{\theta,0}^{\text{est}}$ is set to zero. Figure A.4 shows the estimated circumferential stress. $\sigma_{\theta\theta}^{\text{est}}$, which is obtained from Eqs. (34)–(39), is not consistent with $\sigma_{\theta\theta}$. In contrast, $\sigma_{\theta\theta}^{\text{est,m}}$, which is obtained from Eqs. (36)–(39) with the estimated displacement regarded as the displacement of the middle surface, is relatively consistent with $\sigma_{\theta\theta}$. The maximum value of $\sigma_{\theta\theta}^{\text{est,m}}$ is approximately 88% of that of $\sigma_{\theta\theta}$.

Figure A.5 shows estimated solutions for $E_g = 3.0$ GPa, which is 10 times that of the basic case. There is no difference in the distribution of u_r and u_r^{est}. The difference in the distributions of u_θ and u_θ^{est} for $E_g = 3.0$ GPa is greater than that for $E_g = 0.3$ GPa, and u_θ^{est} is closer to $u_{\theta,\text{mid}}$ than to u_θ. The maximum value of $\sigma_{\theta\theta}^{\text{est,m}}$ is approximately 77% of that of $\sigma_{\theta\theta}$, and the estimation accuracy is lower than that for $E_g = 0.3$ GPa.

Figure A.6 shows estimated solutions under the full-slip condition. The given solutions and the estimated solutions are in agreement when the estimated circumferential displacement is regarded as that of the middle surface, instead of that of the inner surface.

Figure A.7 shows the normalized stress of the inner surface for various values of the Young's modulus of the ground, E_g. The maximum value of $\sigma_{\theta\theta}^{\mathrm{est,m}}$ is divided by that of $\sigma_{\theta\theta}$ to evaluate the estimation accuracy. When the no-slip condition is imposed on the ground–lining interface, the normalized stress becomes less than 1 as E_g increases. In contrast, when the full-slip condition is imposed, the normalized stress remains close to 1, regardless of E_g.

Figure A.8 shows the normalized stress of the inner surface for various lateral pressure coefficients k. When the no-slip condition is imposed, the normalized stress decreases as the value of k deviates from 1. The minimum stress occurs when $k = -1$. In contrast, when the full-slip condition is imposed, the normalized stress remains close to 1 and is independent of k.

We have so far considered the deformation of the lining into an oval shape. In the following, we consider the case where there is a void behind the lining, which can produce more complex deformation under a far-field stress state defined by the vertical component p and horizontal component kp. The void is treated as a partially non-contact boundary between the lining and the ground (Yasuda et al., 2017), and is assumed to range from $\theta = 60°$–$120°$. The first 51 terms of the series (the upper limit of summation N is assumed to be 50 in Eqs. (19) and (20)) are used to obtain the converged theoretical solutions.

Figure A.9 shows the estimated solutions when the no-slip condition is imposed on the ground–lining interface. The accuracy and trends of the estimated solutions when there is a void are basically the same as when there is no void. It can be estimated well even when the complicated deformation occurs. The estimated displacement vector is shifted in a clockwise direction, despite being measured at the center of the tunnel. The estimation accuracy of the circumferential displacement can be improved by ignoring the rigid body rotation component.

Figure A.10 shows the estimated circumferential stress in the case of large vertical loading p. The full-slip condition is imposed on the ground–lining interface. An unrealistically large loading is applied for the purpose of this example. There is almost no difference between $\sigma_{\theta\theta}$ for $p = 0.10$ MPa, $\sigma_{\theta\theta}^{\mathrm{est,m}}$ for $p = 0.10$ MPa, and $\sigma_{\theta\theta}^{\mathrm{est,m}}/10$ for $p = 1.00$ MPa. There is a slight difference between $\sigma_{\theta\theta}^{\mathrm{est,m}}$ for $p = 0.10$ MPa and $\sigma_{\theta\theta}^{\mathrm{est,m}}/100$ for $p = 10.0$ MPa.

Figure A.11 shows the estimated circumferential stress when the measurement position O^{obs} is changed. The measurement position before deformation is (0, 0) and that after deformation is (-3, -3). When the total number of measurement points K is 1001, there is a slight difference between $\sigma_{\theta\theta}$ and

$\sigma_{\theta\theta}^{\mathrm{est,m}}$. The estimation accuracy becomes lower when the measurement position is changed, as shown by a comparison with Fig. A.10. Nevertheless, when the total number of measurement points K is 10001, the estimation error is almost eliminated.

In the actual measurements, errors occur when measuring the distance R^{obs}. Figure A.12 shows an example of the measurement results after deformation when considering the distance measurement error. The total number of measurement points K is 10001. The measurement error is assumed to be a random error following a normal distribution with a mean of zero and standard deviation σ of 0.3 (mm). Thus, the maximum distance measurement error is approximately 1 mm. The deformation and the measurement error are magnified by a factor of 500. The smoothed results of the moving average are also plotted; each moving average result comes from the unweighted mean of the previous 50 and next 50 points (i.e., a total of 101 points and equivalent to 3.6° in the circumferential direction). Figure A.13 shows the estimated solutions. The estimated stress series only includes 11 terms (N is assumed to be 10 in Eqs. (32) and (33)) to prevent the solution from diverging. The maximum error without smoothing of the estimated radial displacement is less than 1σ (=0.3 mm). In contrast, that of the estimated circumferential displacement is considerably larger than 1σ. Smoothing significantly improves the estimation accuracy of the circumferential displacement. The stress can be estimated with a certain degree of accuracy when smoothing is applied. Figure A.14 shows the magnitude of each term of the Fourier series, allowing the contribution of each term to be estimated. Small errors in displacement translate to large errors in stress, especially in the higher-order terms.

4. Discussion

There is almost no error in the estimation of radial displacement, regardless of the conditions, as shown in Figs. A.3, A.5, A.6, and A.9. In contrast, there are persistent errors in the estimation of circumferential displacement. Errors in the circumferential direction are inevitable because the circumferential displacement does not contribute to changes in the outline of a circular tunnel. Basically, the tunnel deformation cannot be accurately estimated using only the point cloud data obtained by distance measurements.

The errors produced by clockwise or counterclockwise rigid body rotation are noticeable because we have assumed that the tunnel cross-section is circular. Generally, the tunnel is surrounded by the ground, and no rigid body rotation occurs. Therefore, the component that contributes to the rigid body rotation $U_{\theta,0}^{\text{est}}$ should be set to zero when estimating the deformation. Indeed, this works well, as shown in Figs. A.3 and A.9.

As a special case, when the full-slip condition is imposed and the estimated circumferential displacement of the inner surface is regarded as that of the middle surface, there is almost no error in the estimation, including that of the circumferential stress, as shown in Fig. A.6. This is because the assumptions of the proposed estimation method and that of the full-slip condition are compatible. The proposed estimation method assumes that the relative position on the closed line is the same before and after tunnel deformation, as mentioned in Section 2.4. In the case of the full-slip condition, the same condition holds on the middle surface, as shown in Section Appendix A. In addition, the radial displacement does not change in the thickness direction, as shown by Eq. (34), and the radial displacement of the inner surface and that of the middle surface are the same and can be estimated accurately. These facts explain why there is almost no error in the estimation under the full-slip condition.

When the no-slip condition is imposed, lower values of the Young's modulus of the ground produce more accurate circumferential stress estimations, as shown in Fig. A.7. This is because the difference in the deformation patterns under the no-slip and full-slip conditions becomes smaller as the Young's modulus of the ground decreases, as shown in Fig. A.15. The $U_{r,2}^{c}$ and $U_{\theta,2}^{s}$ are defined by Eqs. (19) and (20). Specifically, the difference becomes smaller as the relative stiffness of the lining with respect to the ground increases. This can be confirmed from the numerical results shown in Fig. A.16 for a thin lining. Considering the influence of the lateral pressure coefficient k, as this parameter becomes closer to 1, the estimation accuracy improves, as shown in Figs. A.8 and A.16. This is because only radial displacement occurs, and there is no estimation error when $k = 1$.

In general, when there is a high possibility of tunnel deformation, the surrounding ground tends to be soft. In such cases, the lateral pressure coefficient is expected to be close to one, and the relative stiffness of the lining with respect to the ground is high. Therefore, the estimated tunnel deformation is expected to be highly accurate.

The magnitude of tunnel deformation is less sensitive to the estimation accuracy, although the estimation accuracy decreases slightly under large loading magnitudes, as shown in Fig. A.10. In addition, the measurement position and the number of measurement points are less sensitive to the accuracy, as shown in Figs. A.3 and A.11. Sufficient accuracy can be obtained even with 1001 measurement points at irregular intervals.

When errors in the distance measurements are considered, the estimate accuracy decreases, as shown in Figs. A.13 and A.14. This is especially noticeable in the estimation of the circumferential displacement. As the circumferential displacement is not actually measured, the error is likely to be greater than that of the radial displacement. The estimation accuracy decreases as the ratio of the measurement error to the distance between two adjacent measurement points increases, as predicted by Eqs. (26) and (27). Hence, increasing the number of measurement points does not always improve the estimation accuracy. Deformation estimation accuracy may be improved by reducing the number of data used. In this example, the standard deviation of the error is 0.3 mm and the distance between the two points is approximately 3 mm. When considering the distance measurement errors, methods of reducing the size of the error, such as smoothing, should be considered. The estimation accuracy of the displacement can be significantly improved by smoothing, and high accuracy can be achieved when the measurement error is small compared with the tunnel deformation. However, small errors in displacement correspond to significant errors in stress in the higher-order terms of the Fourier series. Therefore, only the lower-order terms can be used for the circumferential stress estimation when considering the measurement error.

Based on the above considerations, the applicability of the proposed method for a circular tunnel has been demonstrated. The advantage of this method is its wide applicability and high accuracy. The proposed method can handle more complicated deformations compared with other deformation evaluation methods, where the ovaling deformation is assumed (Walton et al., 2014; Xie and Lu, 2017; Cui et al., 2019). Moreover, compared with the minimum-distance projection algorithm (Han et al., 2013b,a), which assumed the measurement point after deformation has moved in the normal direction from the estimated surface, this method can estimate the deformation more accurately, as can be predicted from the tunnel deformation in Fig. A.2.

5. Conclusions

This paper has proposed a deformation estimation method from point cloud using EFA. The applicability of the method for a circular tunnel cross-section was demonstrated under several theoretical considerations. The following conclusions can be drawn from this study:

(1) When considering no error in the distance measurements, there is almost no error in the estimation of radial displacement, regardless of the measurement conditions. In contrast, there is some inherent error in the estimation of circumferential displacement because this does not contribute to the change in the outline of a circular tunnel.

(2) The estimation accuracy of the tunnel deformation is expected to be high in tunnels where there is a high possibility of deformation.

(3) When considering errors in the distance measurements, the estimation accuracy of the displacement can be significantly improved by smoothing, and highly accurate estimates can be achieved when the measurement error is small compared with the tunnel deformation.

(4) Only the lower-order terms of the Fourier series can be used for the circumferential stress estimation when considering the measurement error.

Appendix A. Lining deformation when the full-slip condition is imposed on the ground–lining interface

Consider the change in distance between two points on the middle surface of the lining before and after tunnel deformation, as shown in Figure (A.17). $\Delta\ell_1$ is defined as the distance between two points $(R_{\text{mid}}\cos\theta,\, R_{\text{mid}}\sin\theta)$ and $(R_{\text{mid}}\cos(\theta+d\theta),\, R_{\text{mid}}\sin(\theta+d\theta))$, and can be expressed as follows:

$$\Delta\ell_1 \approx R_{\text{mid}} d\theta. \tag{A.1}$$

$\Delta\ell_2$ is defined as the distance between the two points $(R_{\text{mid}}\cos\theta + u_x(\theta),\, R_{\text{mid}}\sin\theta + u_y(\theta))$ and $(R_{\text{mid}}\cos(\theta+d\theta) + u_x(\theta+d\theta),\, R_{\text{mid}}\sin(\theta+d\theta) + u_y(\theta+d\theta))$, and can be expressed as follows:

$$\Delta\ell_2 \approx R_{\text{mid}} d\theta \left\{ 1 + \frac{1}{R_{\text{mid}}} \left(-\frac{du_x}{d\theta}\sin\theta + \frac{du_y}{d\theta}\cos\theta \right) \right\}. \tag{A.2}$$

For simplicity, consider only the deformation components of the n-th term that are symmetric to the y-axis, expressed as follows:

$$u_{r,\mathrm{mid}} = U_{r,n} \cos n\theta, \tag{A.3}$$

$$u_{\theta,\mathrm{mid}} = U_{\theta,n} \sin n\theta. \tag{A.4}$$

After transforming the coordinates, the following equations can be obtained:

$$u_{x,\mathrm{mid}} = \left(\frac{U_{r,n}}{2} + \frac{U_{\theta,n}}{2}\right)\cos(n+1)\theta + \left(\frac{U_{r,n}}{2} - \frac{U_{\theta,n}}{2}\right)\cos(n-1)\theta, \tag{A.5}$$

$$u_{y,\mathrm{mid}} = \left(\frac{U_{r,n}}{2} + \frac{U_{\theta,n}}{2}\right)\sin(n+1)\theta - \left(\frac{U_{r,n}}{2} - \frac{U_{\theta,n}}{2}\right)\sin(n-1)\theta. \tag{A.6}$$

Substituting Eqs. (A.5) and (A.6) into Eq. (A.2) and rearranging, $\Delta\ell_2$ can be expressed as follows:

$$\Delta\ell_2 \approx R_{\mathrm{mid}} d\theta \left\{1 + \frac{1}{R_{\mathrm{mid}}}(U_{r,n} + nU_{\theta,n})\cos n\theta\right\}. \tag{A.7}$$

The surface loading acting on the lining can be expressed as follows:

$$f_r = F_{r,n} \cos n\theta, \tag{A.8}$$

$$f_\theta = F_{\theta,n} \sin n\theta. \tag{A.9}$$

The coefficients $U_{r,n}$, $U_{\theta,n}$ and $F_{r,n}$, $F_{\theta,n}$ have the relationship (Yasuda et al., 2017):

$$\begin{pmatrix} F_{r,n} \\ F_{\theta,n} \end{pmatrix} = \begin{pmatrix} \frac{D_\ell}{R_{\mathrm{mid}}^2} + \frac{K_\ell}{R_{\mathrm{mid}}^4}(n^2-1)^2 & n\frac{D_\ell}{R_{\mathrm{mid}}^2} \\ n\frac{D_\ell}{R_{\mathrm{mid}}^2} & n^2\frac{D_\ell}{R_{\mathrm{mid}}^2} \end{pmatrix} \begin{pmatrix} U_{r,n} \\ U_{\theta,n} \end{pmatrix}. \tag{A.10}$$

When the full-slip condition is imposed on the ground–lining interface, $F_{\theta,n}$ must be equal to zero. Thus, the following equation holds:

$$U_{r,n} + nU_{\theta,n} = 0. \tag{A.11}$$

From a comparison of Eqs. (A.1), (A.7), and (A.11), it is clear that $\Delta\ell_1$ and $\Delta\ell_2$ are equal and the relative position on the closed line is the same before and after the tunnel deformation when the full-slip condition is imposed on the ground–lining interface.

Declaration of Competing Interest

The authors declare that they have no known competing financial interests or personal relationships that could have appeared to influence the work reported in this paper.

References

Cui, H., Ren, X., Mao, Q., Hu, Q., Wang, W., 2019. Shield subway tunnel deformation detection based on mobile laser scanning. Automation in Construction 106, 102889.

Einstein, H.H., Schwartz, C.W., 1979. Simplified analysis for tunnel supports. Journal of the geotechnical engineering division 105, 499–518.

Farahani, B.V., Barros, F., Sousa, P.J., Cacciari, P.P., Tavares, P.J., Futai, M.M., Moreira, P., 2019. A coupled 3d laser scanning and digital image correlation system for geometry acquisition and deformation monitoring of a railway tunnel. Tunnelling and Underground Space Technology 91, 102995.

Fekete, S., Diederichs, M., Lato, M., 2010. Geotechnical and operational applications for 3-dimensional laser scanning in drill and blast tunnels. Tunnelling and underground space technology 25, 614–628.

Flügge, W., 1973. Stress in Shells. Berlin and New York: Springer-Verlag.

Han, J.Y., Guo, J., Jiang, Y.S., 2013a. Monitoring tunnel deformations by means of multi-epoch dispersed 3d lidar point clouds: An improved approach. Tunnelling and Underground Space Technology 38, 385–389.

Han, J.Y., Guo, J., Jiang, Y.S., 2013b. Monitoring tunnel profile by means of multi-epoch dispersed 3-d lidar point clouds. Tunnelling and underground space technology 33, 186–192.

Jiang, Q., Zhong, S., Pan, P.Z., Shi, Y., Guo, H., Kou, Y., 2020. Observe the temporal evolution of deep tunnel's 3d deformation by 3d laser scanning in the jinchuan no. 2 mine. Tunnelling and Underground Space Technology 97, 103237.

Kuhl, F.P., Giardina, C.R., 1982. Elliptic fourier features of a closed contour. Computer graphics and image processing 18, 236–258.

Lato, M.J., Diederichs, M.S., 2014. Mapping shotcrete thickness using lidar and photogrammetry data: Correcting for over-calculation due to rockmass convergence. Tunnelling and Underground Space Technology 41, 234–240.

Lestrel, P.E., 1989. Method for analyzing complex two-dimensional forms: Elliptical fourier functions. American Journal of Human Biology 1, 149–164.

Nuttens, T., Stal, C., De Backer, H., Schotte, K., Van Bogaert, P., De Wulf, A., 2014. Methodology for the ovalization monitoring of newly built circular train tunnels based on laser scanning: Liefkenshoek rail link (belgium). Automation in construction 43, 1–9.

Puente, I., Akinci, B., González-Jorge, H., Díaz-Vilariño, L., Arias, P., 2016. A semi-automated method for extracting vertical clearance and cross sections in tunnels using mobile lidar data. Tunnelling and underground space technology 59, 48–54.

Timoshenko, S.P., Goodier, J.N., 1951. Theory of elasticity .

Walton, G., Delaloye, D., Diederichs, M.S., 2014. Development of an elliptical fitting algorithm to improve change detection capabilities with applications for deformation monitoring in circular tunnels and shafts. Tunnelling and Underground Space Technology 43, 336–349.

Xie, X., Lu, X., 2017. Development of a 3d modeling algorithm for tunnel deformation monitoring based on terrestrial laser scanning. Underground Space 2, 16–29.

Xie, X., Tian, H., Zhou, B., Li, K., 2021. The life-cycle development and cause analysis of large diameter shield tunnel convergence in soft soil area. Tunnelling and Underground Space Technology 107, 103680.

Xu, J., Ding, L., Luo, H., Chen, E.J., Wei, L., 2019. Near real-time circular tunnel shield segment assembly quality inspection using point cloud data: A case study. Tunnelling and Underground Space Technology 91, 102998.

Yasuda, N., Tsukada, K., Asakura, T., 2017. Elastic solutions for circular tunnel with void behind lining. Tunnelling and Underground Space Technology 70, 274–285.

Yoon, J.S., Sagong, M., Lee, J., Lee, K.s., 2009. Feature extraction of a concrete tunnel liner from 3d laser scanning data. Ndt & E international 42, 97–105.

Table A.1: Material properties.

Parameters	Ground	Lining
Young's modulus (GPa)	0.01-10	30
Poisson's ratio	0.30	0.20
Inner radius R (m)		5.0
Lining thickness h (m)		0.50

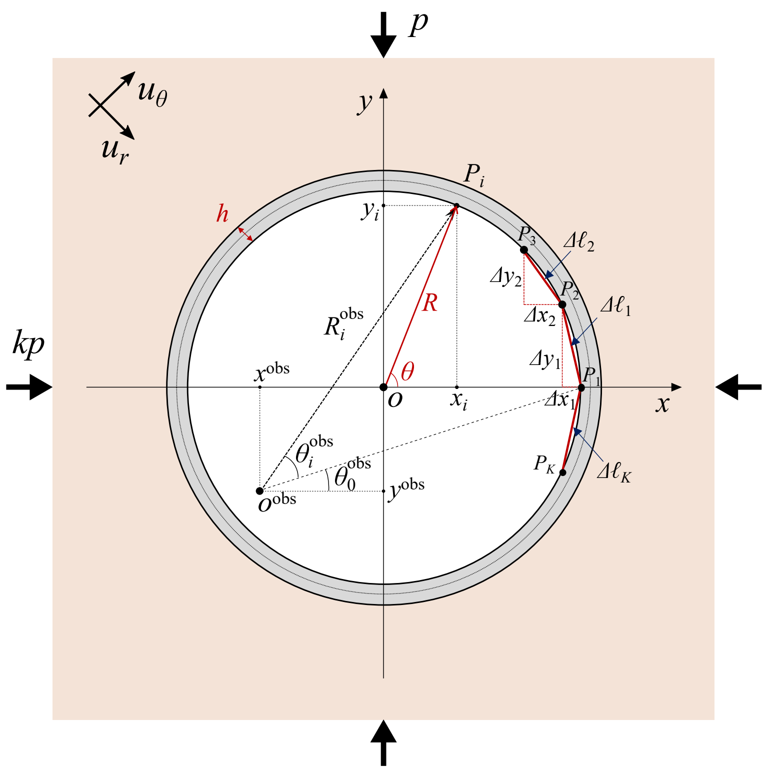

Figure A.1: Problem geometry with measurement points.

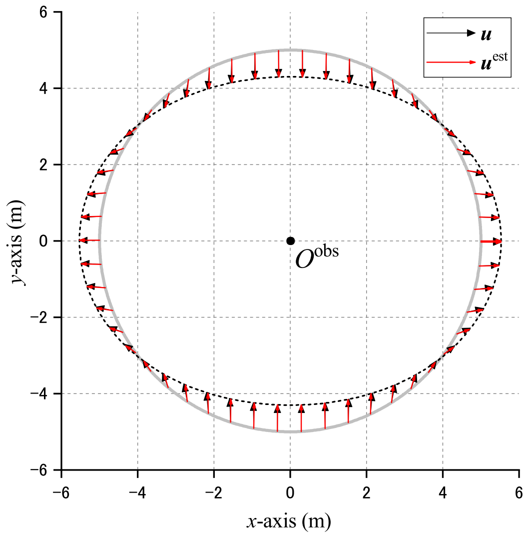

(a)

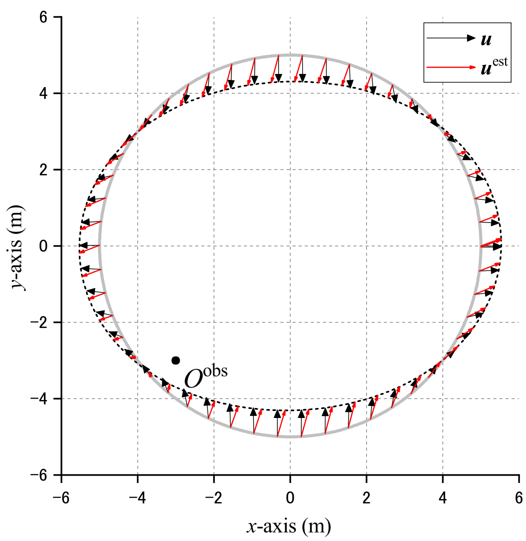

(b)

Figure A.2: Estimated displacement distribution for (a) $O^{\text{obs}}(0, 0)$ and (b) $O^{\text{obs}}(-3, -3)$ (with $E_g = 0.30$ GPa, $p = 0.10$ MPa, $k = 0.50$, $K = 1001$, and the no-slip condition). The displacement is magnified by a factor of 500.

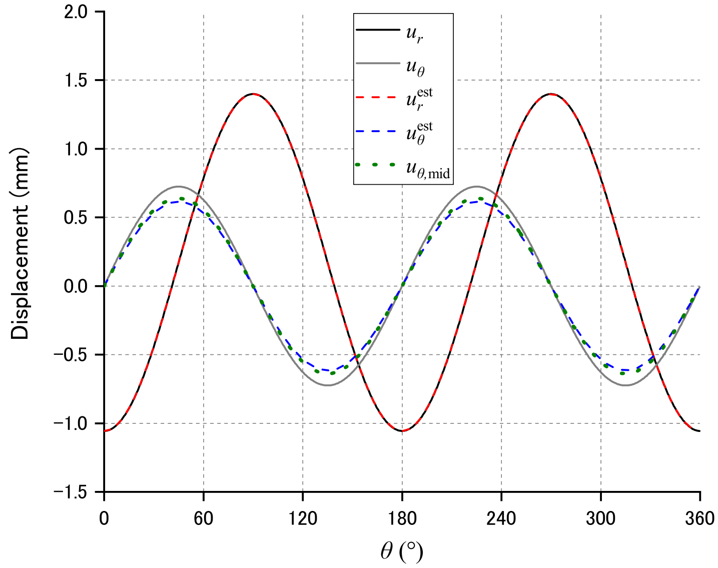

(a)

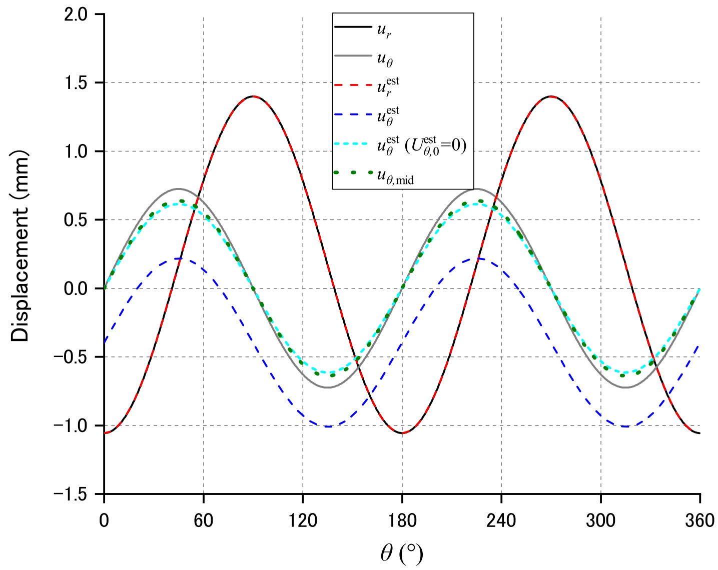

(b)

Figure A.3: Estimated radial and circumferential displacement for (a) $O^{\mathrm{obs}}(0, 0)$ and (b) $O^{\mathrm{obs}}(-3, -3)$.

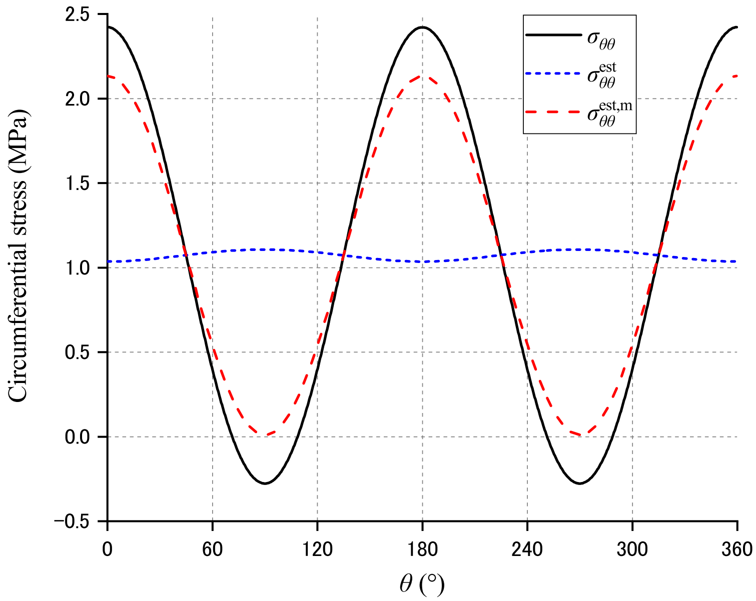

Figure A.4: Estimated circumferential stress of the inner surface for $O^{\mathrm{obs}}(-3, -3)$.

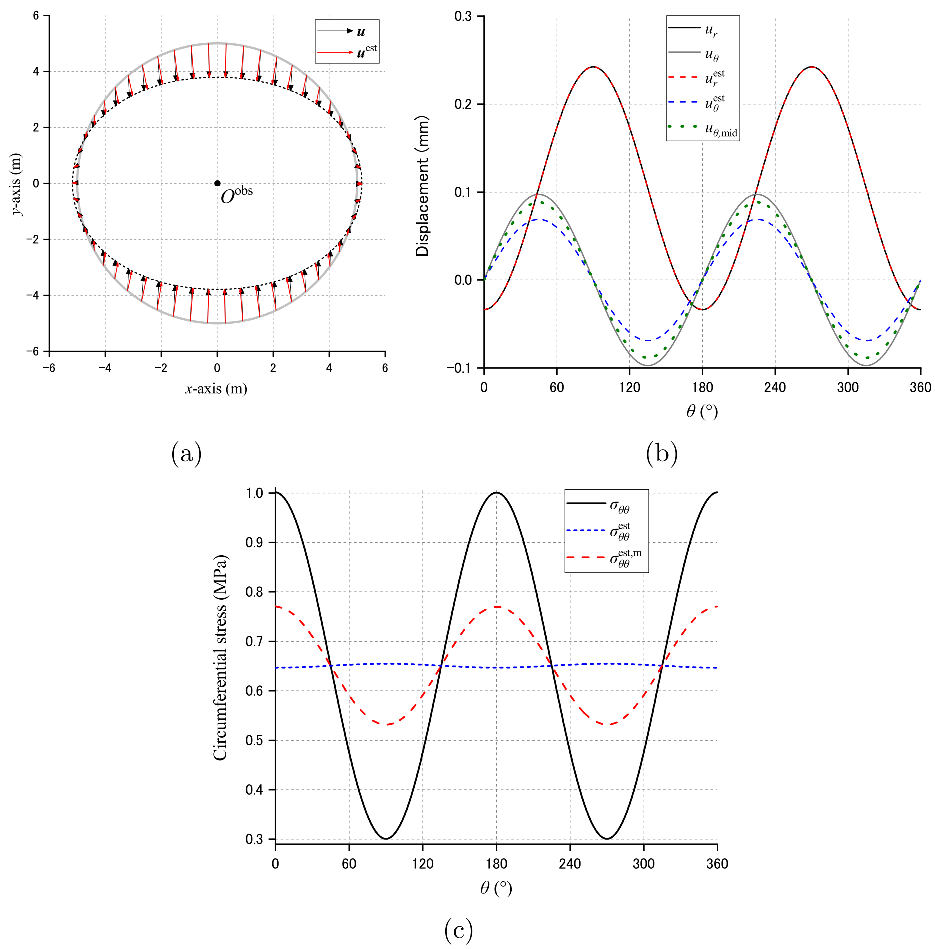

Figure A.5: Estimated solutions for $E_g = 3.0$ GPa (with $p = 0.10$ MPa, $k = 0.50$, $K = 1001$, $O^{\text{obs}}(0,0)$, and the no-slip condition): (a) displacement distribution, where the displacement is magnified by a factor of 5000, (b) radial and circumferential displacement, and (c) circumferential stress of the inner surface.

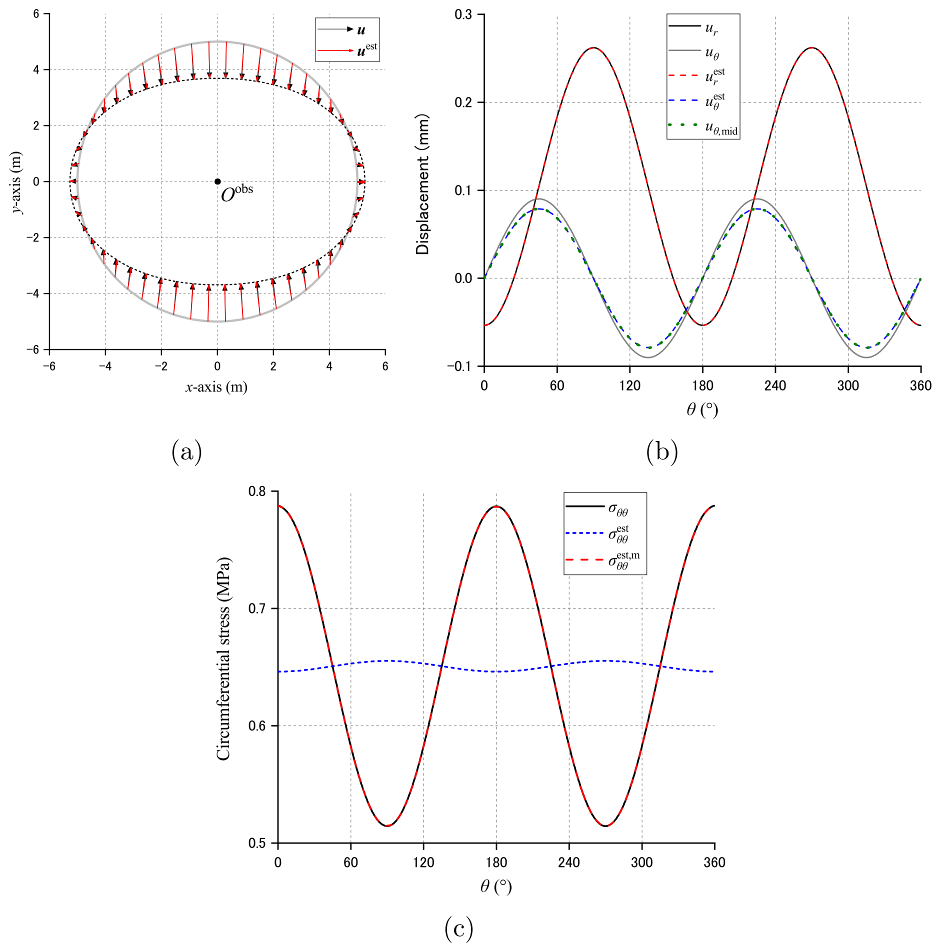

Figure A.6: Estimated solutions under the full-slip condition (with $E_g = 3.0$ GPa, $p = 0.10$ MPa, $k = 0.50$, $K = 1001$, and $O^{\mathrm{obs}}(0,0)$): (a) displacement distribution, where the displacement is magnified by a factor of 5000, (b) radial and circumferential displacement, and (c) circumferential stress of the inner surface.

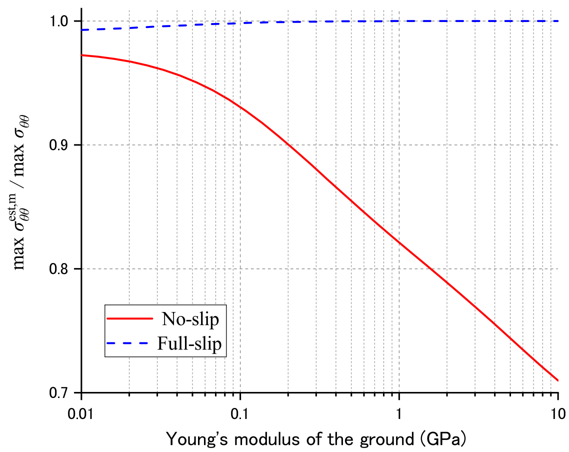

Figure A.7: Normalized stress of the inner surface for various values of Young's modulus of the ground E_g (with $p = 0.10$ MPa, $k = 0.50$, $O^{\mathrm{obs}}(0,0)$, and $K = 1001$).

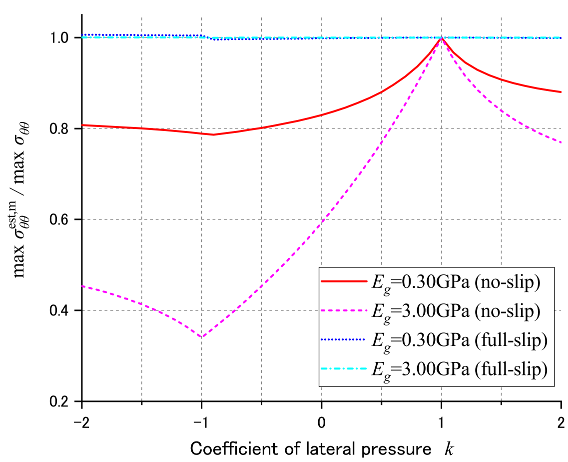

Figure A.8: Normalized stress of the inner surface stress for various lateral pressure coefficients k (with $p = 0.10$ MPa, $K = 1001$, and $O^{\mathrm{obs}}(0,0)$).

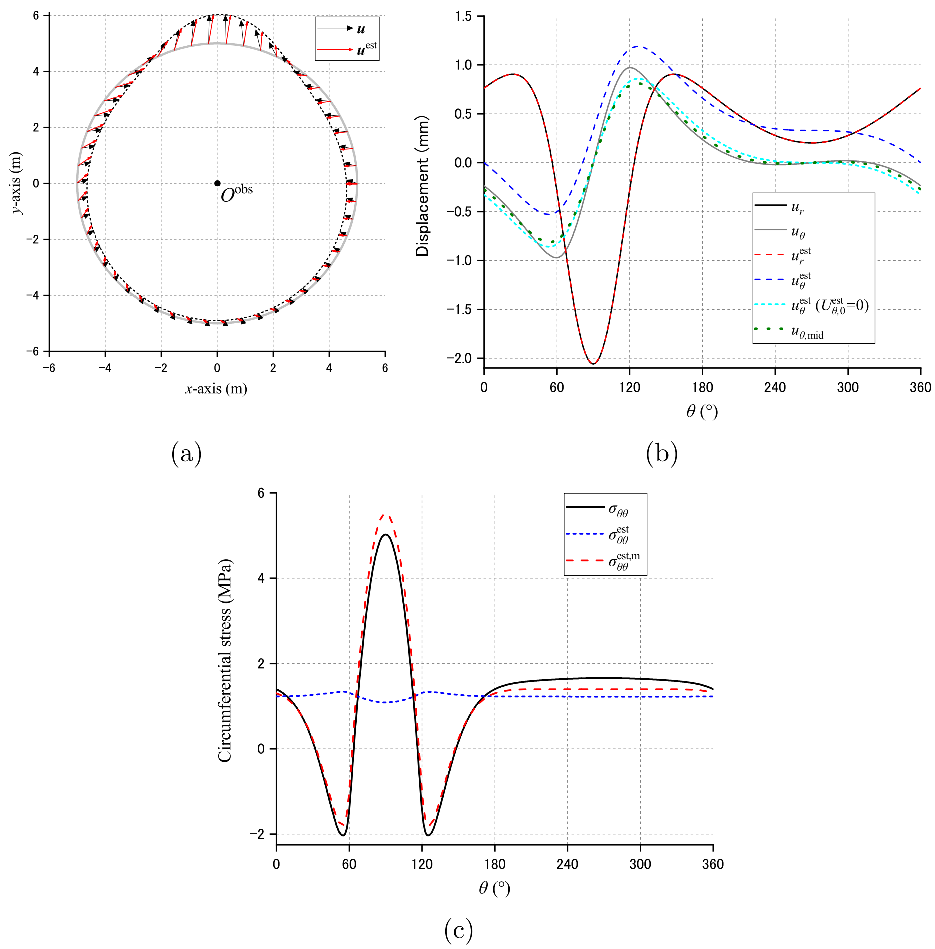

(a) (b) (c)

Figure A.9: Estimated solutions when there is a void behind the lining (with $E_g = 0.3$ GPa, $p = 0.10$ MPa, $k = 1.00$, $K = 1001$, $O^{\text{obs}}(0, 0)$, and the no-slip condition): (a) displacement distribution, where the displacement is magnified by a factor of 500, (b) radial and circumferential displacement, and (c) circumferential stress of the inner surface.

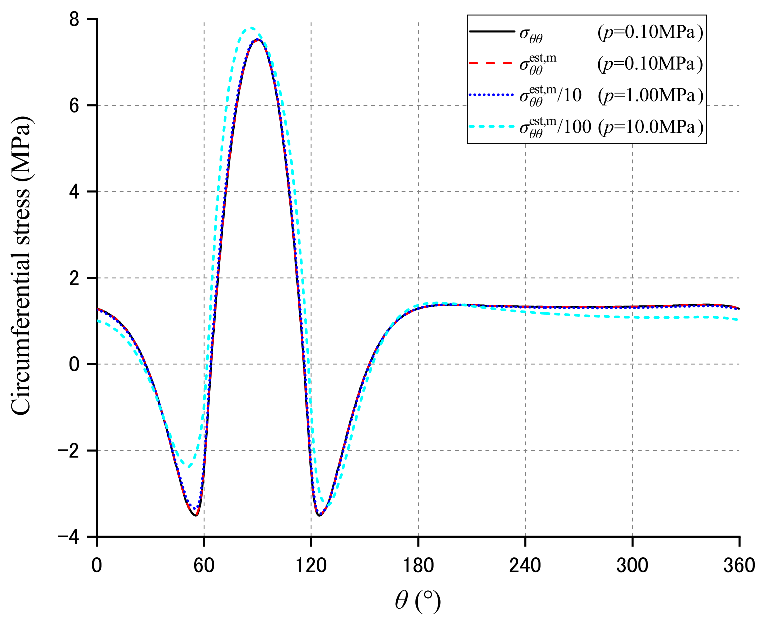

Figure A.10: Estimated circumferential stress of the inner surface for large vertical loading (with $E_g = 0.3$ GPa, $k = 1.00$, $K = 1001$, $O^{\mathrm{obs}}(0, 0)$, the full-slip condition, and a void behind the lining).

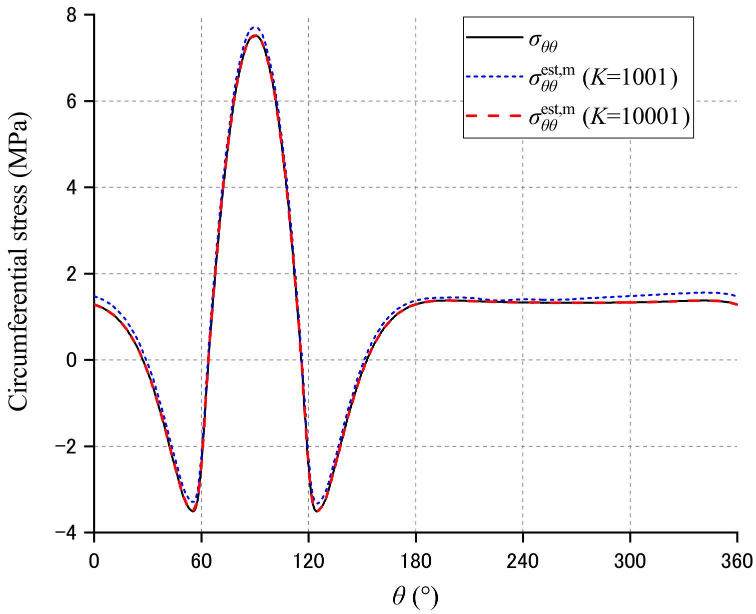

Figure A.11: Estimated circumferential stress of the inner surface when the measurement position O^{obs} is (0, 0) before the deformation and (-3, -3) after the deformation (with E_g = 0.30 GPa, p = 0.10 MPa, k = 1.00, the full-slip condition, and a void behind the lining).

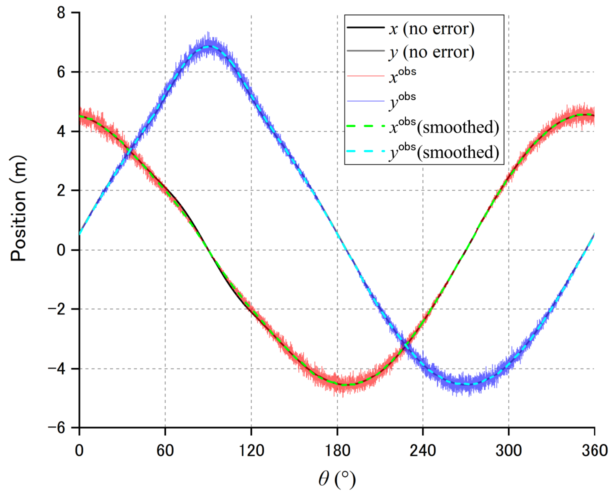

Figure A.12: Example of measurement results after deformation when considering the distance measurement error (with $E_g = 0.30$ GPa, $p = 0.10$ MPa, $k = 1.00$, $K = 10001$, $O^{\mathrm{obs}}(0,\, 0)$, the full-slip condition, and a void behind the lining). The measurement error follows a normal distribution with a mean of zero and standard deviation of 0.3 (mm). The deformation and the measurement error are magnified by a factor of 500.

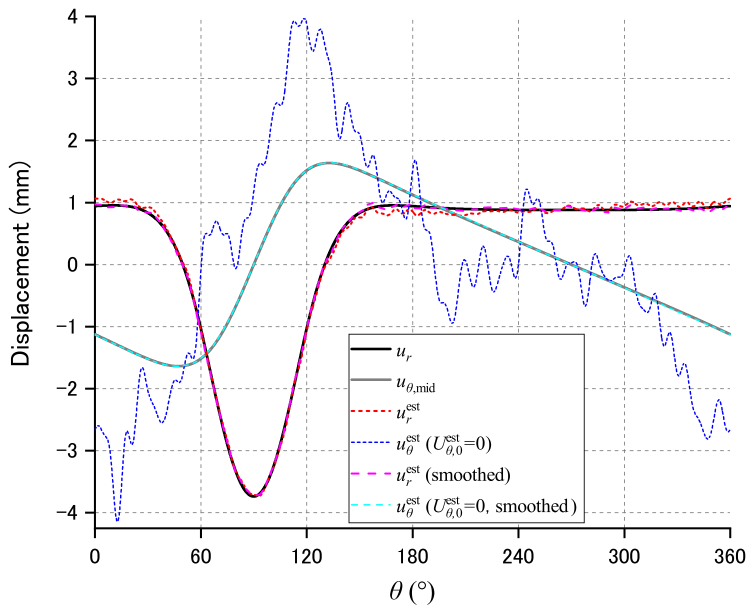

(a)

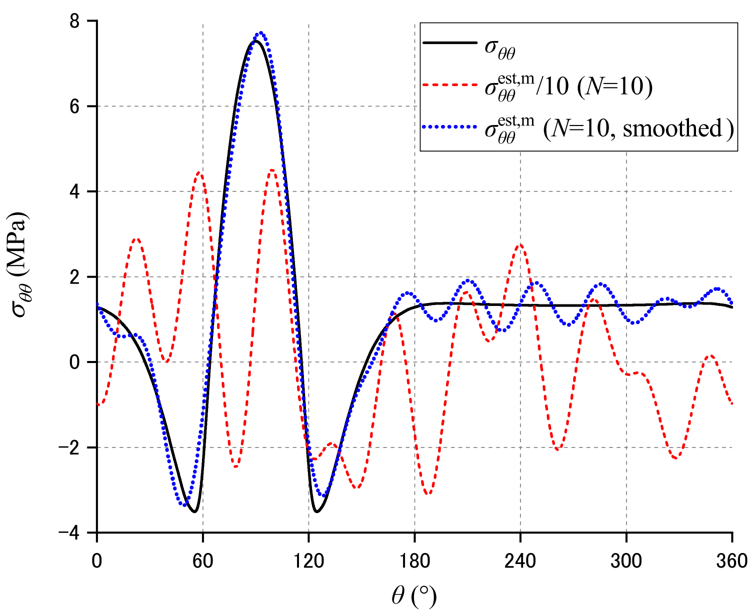

(b)

Figure A.13: Estimated solutions when considering the distance measurement error: (a) radial and circumferential displacement and (b) circumferential stress of the inner surface.

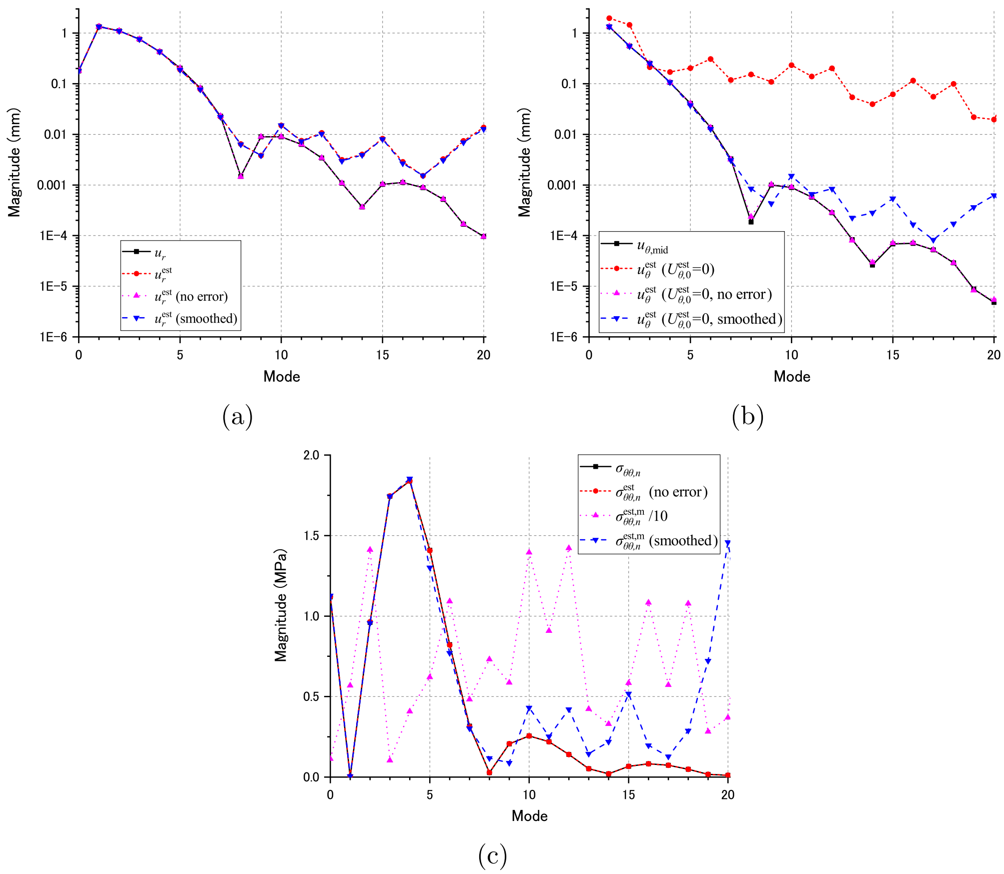

Figure A.14: Magnitude of each term of the Fourier series when considering the distance measurement error: (a) radial displacement, (b) circumferential displacement, and (c) circumferential stress of the inner surface.

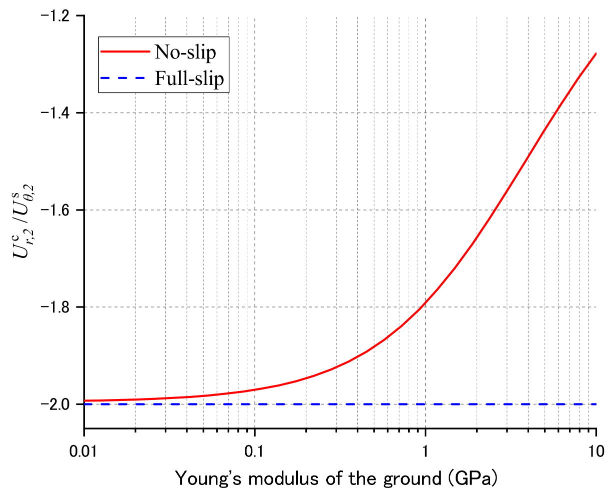

Figure A.15: Relative value of $U^c_{r,2}$ for $U^s_{\theta,2}$ for various values of the Young's modulus of the ground E_g.

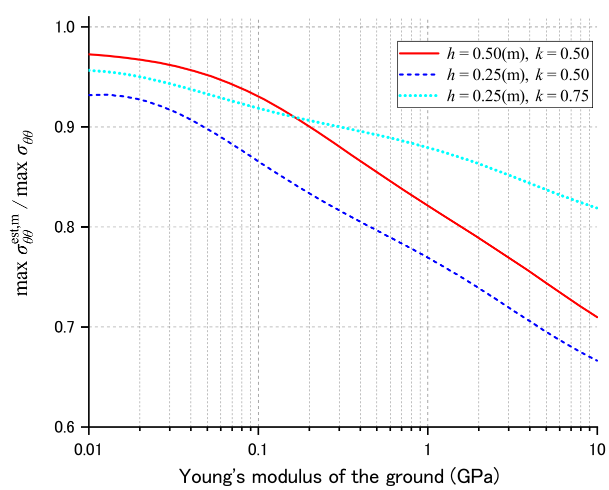

Figure A.16: Normalized stress of the inner surface for a thin lining (with $p = 0.10$ MPa, $K = 1001$, $O^{\mathrm{obs}}(0, 0)$, the no-slip condition, and no void behind the lining).

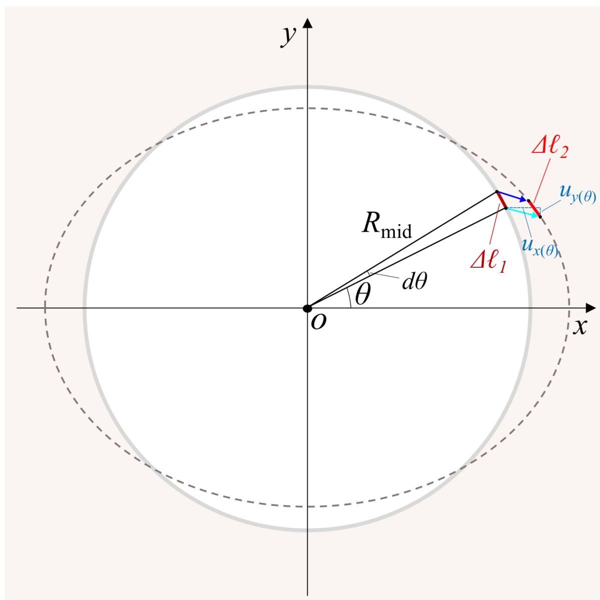

Figure A.17: Schematic diagram of the change in distance between two points on the middle surface of the lining before and after tunnel deformation.